Nanoscale

PAPER

View Article Online
View Journal | View Issue

Cite this: *Nanoscale*, 2015, **7**, 3002

Origin of the large dispersion of magnetic properties in nanostructured oxides: Fe_xO/Fe_3O_4 nanoparticles as a case study†

Marta Estrader,*[a,b] Alberto López-Ortega,[c] Igor V. Golosovsky,*[d,e] Sònia Estradé,[f] Alejandro G. Roca,[g] German Salazar-Alvarez,[b] Lluís López-Conesa,[f] Dina Tobia,[h] Elin Winkler,[h] José D. Ardisson,[i] Waldemar A. A. Macedo,[i] Andreas Morphis,[j] Marianna Vasilakaki,[j] Kalliopi N. Trohidou,[j] Arsen Gukasov,[k] Isabelle Mirebeau,[k] O. L. Makarova,[l] Roberto D. Zysler,[h] Francesca Peiró,[f] Maria Dolors Baró,[m] Lennart Bergström[b] and Josep Nogués[g,n]

The intimate relationship between stoichiometry and physicochemical properties in transition-metal oxides makes them appealing as tunable materials. These features become exacerbated when dealing with nanostructures. However, due to the complexity of nanoscale materials, establishing a distinct relationship between structure-morphology and functionalities is often complicated. In this regard, in the Fe_xO/Fe_3O_4 system a largely unexplained broad dispersion of magnetic properties has been observed. Here we show, thanks to a comprehensive multi-technique approach, a clear correlation between the magneto-structural properties in large (45 nm) and small (9 nm) Fe_xO/Fe_3O_4 core/shell nanoparticles that can explain the spread of magnetic behaviors. The results reveal that while the Fe_xO core in the large nanoparticles is antiferromagnetic and has bulk-like stoichiometry and unit-cell parameters, the Fe_xO core in the small particles is highly non-stoichiometric and strained, displaying no significant antiferromagnetism. These results highlight the importance of ample characterization to fully understand the properties of nanostructured metal oxides.

Received 28th October 2014,
Accepted 29th December 2014

DOI: 10.1039/c4nr06351a

www.rsc.org/nanoscale

Introduction

Transition metal oxides are extremely versatile given the well-established dependence of their physicochemical properties on the oxidation state.[1–3] Interestingly, this effect is dramatically enhanced at the nanoscale, since their reactivity may result in local differences in the oxidation state of the material which may lead to novel properties.[4] However, as the size is reduced down to a few nanometers, the characterization of these sophisticated systems should not solely rely on a few techniques as is usually done for bulk materials. Namely, the fine, yet critical, structural alterations which often occur at the nanoscale may be easily overlooked or misinterpreted if not properly analyzed.[5–8] For instance, in tantalum oxides TaO_{2-x} (Ta^{+4}) is conducting whereas Ta_2O_{5-x} (Ta^{+5}) is insulating. Notably, an in-depth electron microscopy analysis demonstrated the presence of a TaO_{1-x} nanoscale layer which was, in part, responsible for the observation of a new resistance-switching phenomenon.[4] A similar case is also found for nanostructured perovskite manganites, where, for example, a gradual transition from antiferromagnetism to ferromagnetism contrasts with the sharp one exhibited in bulk.[9] A widely studied transition metal system is iron oxide, Fe_xO_y.[10–14] Among iron oxide

[a]*Departament de Química Inorgànica, Universitat de Barcelona, Diagonal 645, E-08028 Barcelona, Spain. E-mail: martaestrader@gmail.com*
[b]*Department of Materials and Environmental Chemistry, Arrhenius Laboratory, Stockholm University, 10691 Stockholm, Sweden*
[c]*INSTM and Dipartimento di Chimica "U. Schiff", Università degli Studi di Firenze, Via della Lastruccia 3, Sesto Fiorentino, I-50019 Firenze, Italy*
[d]*National Research Center "Kurchatov Institute", B.P. Konstantinov, St. Petersburg Nuclear Physics Institute, 188300 Gatchina, Russia. E-mail: golosov@pnpi.spb.ru*
[e]*A.F. Ioffe Physico-Technical Institute RAS, 194021 St. Petersburg, Russia*
[f]*LENS-MIND-IN2UB, Departament d'Electrònica, Universitat de Barcelona, Martí i Franquès 1, E-08028 Barcelona, Spain*
[g]*ICN2 – Institut Catala de Nanociencia i Nanotecnologia, Campus UAB, E-08193 Bellaterra (Barcelona), Spain*
[h]*Centro Atómico Bariloche, CNEA-CONICET, 8400 S.C. de Bariloche, Río Negro, Argentina*
[i]*Laboratório de Física Aplicada, Centro de Desenvolvimento da Tecnologia Nuclear, 31270-901Belo Horizonte, Minais Gerais, Brazil*
[j]*INN-Institute of Nanoscience and Nanotechnology, NCSR "Demokritos", 153 10 Aghia Paraskevi, Attiki, Greece*
[k]*Laboratoire Leon Brillouin, CEA/CNRS, F-91191 Gif-sur-Yvette Cedex, France*
[l]*National Research Center "Kurchatov Institute", 123182 Moscow, Russia*
[m]*Departament de Física, Universitat Autònoma de Barcelona, E-08193 Bellaterra (Barcelona), Spain*
[n]*Institució Catalana de Recerca i Estudis Avançats (ICREA), Barcelona, Spain*
†Electronic supplementary information (ESI) available. See DOI: 10.1039/c4nr06351a

materials, wüstite (Fe_xO) is a particularly interesting material. In bulk, wüstite is not stable under ambient conditions and disproportionates into α-Fe and magnetite (Fe_3O_4). However, metastable non-stoichiometric Fe_xO can be obtained by high temperature quenching. Moreover, Fe_xO can be stable in nanoparticle form.[15–18] Fe_xO can oxidize into Fe_3O_4 and subsequently into maghemite (γ-Fe_2O_3), which at the nanoscale may give rise to Fe_xO/Fe_3O_4 core/shell particles.[10,19–37] Fe_xO/Fe_3O_4 systems have been proposed for diverse applications, including magnetic bioassays, microwave absorbers, anode materials for Li-ion batteries or solar hydrogen production *via* water-splitting.[35,38–41]

From a magnetic point of view Fe_xO is antiferromagnetic (AFM) whereas Fe_3O_4 is ferrimagnetic (FiM), which gives rise to a rich set of magnetic properties in this system.[10,19–37] In particular, exchange coupling between the AFM-core and the FiM-shell, which strongly depends on the core size, shell thickness or shape, should result in an exchange bias, *i.e.*, the shift of the hysteresis loop in the field axis after field cooling (H_E).[42–47] Remarkably, in Fe_xO/Fe_3O_4 core/shell nanoparticles an unusually broad spectrum of magnetic properties has been reported, even for nominally comparable particles. For instance, Kavich *et al.* showed an exchange bias in 14 nm Fe_xO/Fe_3O_4 particles whereas the ones of 13 nm reported by Lak *et al.* show $H_E = 0$, thus claiming the absence of a Fe_xO core.[22,27] On the other hand, an exchange bias was observed in single phase $Fe_{3-\delta}O_4$ nanoparticles, after the complete oxidation of the Fe_xO phase, which was ascribed to the presence of antiphase boundaries formed during the oxidation process. These antiphase boundaries were also claimed to be responsible for the observed reduced saturation magnetization (M_S) compared to bulk values, although Benitez *et al.* attributed an analogous M_S reduction (in similar 20 nm particles) to the occurrence of small amounts of Fe_xO.[25,32] Further, some groups report obvious features of the Fe_xO AFM transition at its Néel temperature, T_N (*e.g.*, a sharp downturn of magnetization around T_N) while others find the temperature dependence of magnetization, $M(T)$, featureless around T_N.[22,27,32,34,36,37] Similarly, although in some cases the nanoparticles have been shown to exhibit a clear Verwey transition, T_V (typical of bulk Fe_3O_4),[28,36] similar particles show no characteristics of this transition.[22,25,27]

To address the origin of these diverse magnetic behaviours, in this work we present an in-depth systematic study of two different Fe_xO/Fe_3O_4 core/shell systems, with significantly different overall sizes of 9 and 45 nm. These particle sizes are among the smallest and largest sizes of core–shell Fe_xO/Fe_3O_4 nanoparticles, respectively, with a well-defined size and shape reported in the literature. Diverse techniques have been employed to accurately characterize both compositionally and magnetically the core/shell structure. The results show that the spread of magnetic responses in the Fe_xO/Fe_3O_4 core/shell systems stems from a combination of factors such as size effects, the composition x of the Fe_xO core or the strains in both the core and the shell.

Results

Structural and morphological characterization

Fig. 1a, b show the transmission electron microscopy (TEM) images of small spherical, CS_9, and large cubic-shaped, CS_45, nanoparticles, respectively. The corresponding volume–weight particle size histograms, depicted in the insets, follow a Gaussian distribution with mean sizes of 9.4(4) nm and 45(6) nm for the CS_9 and CS_45 nanoparticles, respectively. The HRTEM images (insets of Fig. 1a, b) clearly show the crystallinity of the particles, although the presence of a core/shell morphology cannot be completely identified. To elucidate the composition of the nanoparticles, local electron energy loss spectra (EELS) analysis across the whole particle was performed. The Fe/O ratio confirms a core/shell structure (diameter/thickness) of Fe_xO(3 nm)/Fe_3O_4(3.5 nm) for CS_9 and Fe_xO(20 nm)/Fe_3O_4(8 nm) for CS_45 (Fig. 1c, d). Further, the iron oxidation state ($Fe_{ox.st}$) was obtained both for the shell (orange colour in the graphs) and the core (represented in green) by a quantitative analysis of the EELS data (Fig. 1e, f). Note that to obtain the oxidation state of the core the Fe_3O_4-shell contribution was subtracted. As can be seen in Fig. 1e, f, for both the CS_9 and CS_45 particles, in the shell region $Fe_{ox.st}$ is +2.6, which exactly corresponds to Fe_3O_4. In contrast, while for CS_45 particles the Fe_xO-core has an average $Fe_{ox.st}$ = +2.05 which denotes a $Fe_{0.95}O$ composition, the CS_9 particles have a $Fe_{ox.st}$ = +2.2. This implies that the core of the small particles has a highly defected wüstite phase with a $Fe_{0.80}O$ stoichiometry. As shown in the inset of Fig. 1f, the Fe_xO/Fe_3O_4 core/shell structure of the large particles, CS_45, is further confirmed by an EELS mapping using the Fe^{2+} and Fe^{3+} oxidation states.[8]

The profile refinement of the X-ray patterns indicates two dominant phases in the samples: magnetite (Fe_3O_4), with a spinel structure, and wüstite (Fe_xO), with a NaCl structure (Fig. 2). The analysis has also revealed that the CS_45 sample contains some impurities: a small fraction of 7 nm Fe_3O_4 particles and some α-Fe particles (Fig. 2b and ESI Table S1†). To analyze the morphology of the core/shell particles, while the core size is obtained from the crystallite size obtained from the Fe_xO peak broadening, the shell size is the calculated effective thickness of a uniform layer covering the core from the refined scale factors, which are proportional to the scattering volumes. This analysis leads to a Fe_xO-core/Fe_3O_4-shell structure with dimensions of 10.1(5)/2.0(2) nm and 21(1)/8.8(3) nm for CS_9 and CS_45 nanoparticles, respectively, consistent with the microscopy results. The study of the Fe_3O_4-shell composition shows refined oxygen parameter values, 0.252(4)-CS_9 and 0.257(4)-CS_45 and unit cell values, 0.8395(1) nm CS_9 and 0.8391(2) nm CS_45, close to the 0.2548 and 0.8394 nm values of bulk stoichiometric magnetite. This implies that the Fe_3O_4-shell is, in both types of samples, rather stoichiometric (in agreement with EELS). The lattice parameter is very similar to bulk values, but larger than typical values observed in nanoparticles, which may indicate that the Fe_3O_4 may be slightly strained. Owing to the strong correlation between x and the

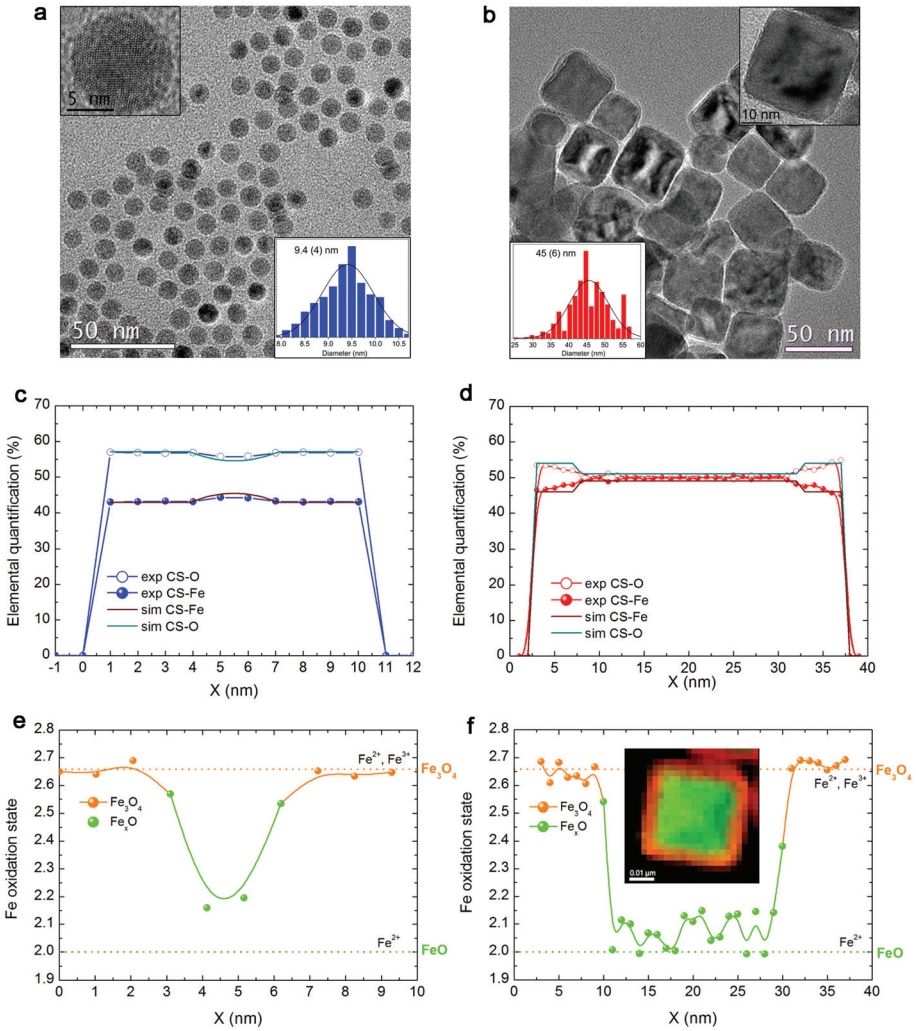

Fig. 1 TEM images of the CS nanoparticles: (a) CS_9 and (b) CS_45. Shown in the insets are the histograms of the corresponding particles (bottom) and HRTEM images of a single particle (top). The number of particles used to obtain the particle size distribution is about 150. Elemental quantification along the particle diameter for Fe (filled circles) and O (empty circles) of (c) CS_9 and (d) CS_45 particles. The solid lines represent the simulated elemental profile for a particle with a Fe_xO-3 nm/Fe_3O_4-3.5 nm and a Fe_xO-20 nm/Fe_3O_4-8 nm core/shell structure for CS_9 and CS_45 particles, respectively. Fe oxidation state along the particle diameter of (e) CS_9 and (f) CS_45 particles. Shown in the inset of (f), is an EELS-mapping of CS_45 nanoparticles (where green corresponds to the O K signal corresponding to Fe_xO and orange to the O K signal of Fe_3O_4 after background subtraction using a power law fit).

Debye factor, to perform the Fe_xO-core profile refinement the x parameter was fixed according to the EELS data of $Fe_{0.80}O$-CS_9 and $Fe_{0.95}O$-CS_45. The lattice parameters obtained from the fit for Fe_xO are rather different for both particles, with 0.42190(8) nm for CS_9 and 0.42986(1) nm for CS_45. Interestingly, given that in bulk Fe_xO the unit cell and the x parameters are directly related by the formula $a_{FexO} = 0.3856 + 0.478x$,[26,48] we have calculated the x values of our particles using the refined unit cell parameters, leading to $Fe_{0.76(1)}O$-CS_9 and $Fe_{0.92(1)}O$-CS_45, which are consistent with the EELS results. The small discrepancy between the x values obtained from EELS and the lattice parameter may indicate that apart from non-stoichiometry, the Fe_xO cell may be compressed with respect to bulk samples with the same x. Unfortunately, given the overlap of the XRD peaks of the two phases the use of the Williams–Hall plot analysis is rather unreliable to obtain information about the strains in the system. Hence, to assess the internal strains in the nanoparticles geometric phase analysis (GPA) was used for the CS_45 particles. Notably, GPA allows for the determination and quantification of crystal lattice deformations from high-resolution TEM images.[25] The strains existing in two different sublattices, *i.e.*, the (220) lattice plane associated with the cations in the tetrahedral positions (spinel phase only) and the (400_{Spinel} and $200_{wüstite}$) lattice plane associated with both the spinel and wüstite phases were studied through the phase imaging of these reflections upon applying GPA (see the Methods section and ESI Fig. S1†). The deformation maps along $\mathbf{g}_{200(wüstite)}/\mathbf{g}_{400(spinel)}$ and $\mathbf{g}_{220(spinel)}$ (Fig. 3a,c) clearly indicate a core with compressive, positive strains and a shell with tensile, negative

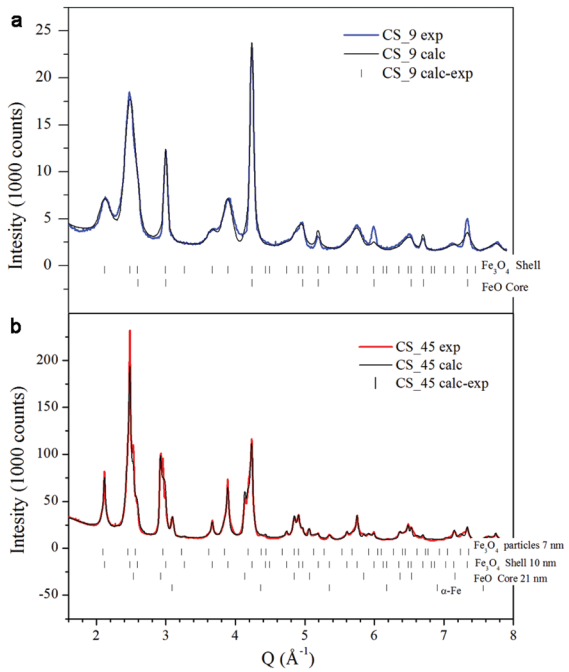

Fig. 2 Profile analysis of the X-ray diffraction patterns from the (a) CS_9 and the (b) CS_45 nanoparticles. The observed profile (blue-CS_9; red-CS_45) and the calculated (in black) are all shown in the graphs. The vertical bars mark the position of the Bragg reflections as indicated.

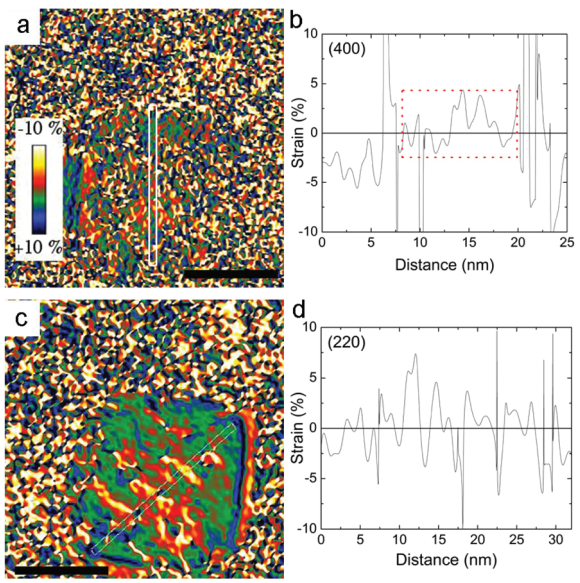

Fig. 3 Deformation maps obtained through the GPA of the (a) $g_{200(wüstite)}/g_{400(spinel)}$ and (c) $g_{220(spinel)}$ reflections for the CS_45 nanoparticles (scale bar = 25 nm). (b) and (d) show the corresponding integrated line profiles. The boxed region in the graph indicates the probable position of the Fe_xO core.

strains. This becomes particularly evident in Fig. 3c; the central part of the particle (*i.e.*, the core) is predominantly red-yellow (compressive strains), whereas the boundary of the particle (*i.e.*, the shell) is mainly green-blue (*i.e.*, expansive strains). The quantification of the strains originating from these defects is shown in Fig. 3b,d. The strain analysis along $g_{200(wüstite)}/g_{400(spinel)}$ (Fig. 3b) unambiguously shows highly strained regions due to mismatch dislocations, which are likely located at the core–shell interface. The stressed interface arises from mismatched dislocations owing to the lattice differences between the wüstite (core) and spinel (shell) phases, as previously demonstrated in this type of system.[25] An analogous study of CS_9 nanoparticles reveals a similar strained structure (see ESI Fig. S2†). However, these particles are exceedingly small to carry out a reliable quantitative GPA analysis.

Neutron diffraction

The magnetic structure of both the Fe_xO-core and the Fe_3O_4-shell for the two core/shell samples was determined by neutron diffraction (ESI Fig. S3†). The refined average magnetic moments in the shell for CS_9 and CS_45 are $3.8(6)\mu_B$ and $4.2(3)\mu_B$, respectively. Concerning the magnetic structure of the Fe_xO-core remarkable opposite features between the CS_9 and CS_45 samples are manifested. Firstly, in the CS_9 particles, the absence of all the expected magnetic reflections

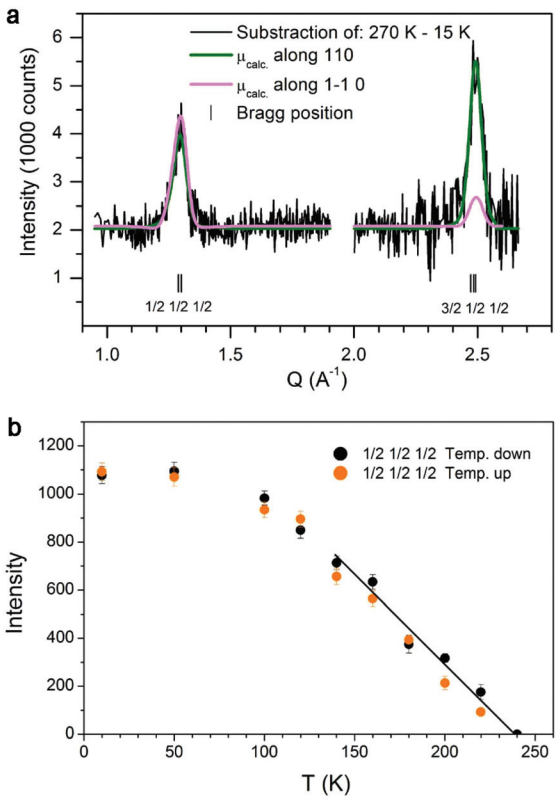

Fig. 4 (a) Difference between neutron diffraction patterns at 270 K and 15 K (in black) for the CS_45 particles. Also shown in the graph are the calculated neutron diffraction patterns considering the magnetic moment aligned along the [110] (in green) and [1–10] (in pink) axes. The vertical bars mark the position of the Bragg reflections as indicated. (b) Temperature dependence of the intensity of the magnetic peak at 1.3 $Å^{-1}$ (corresponding to the (1/2,1/2,1/2) reflection) both while decreasing (in black) and increasing (in orange) the temperature.

indicates a lack of magnetic order in the Fe_xO-core. On the other hand, the scenario for the CS_45 particles is completely different, since not only they present the usual (3/2, 1/2, 1/2) magnetic reflection, but they also exhibit the forbidden (1/2, 1/2, 1/2) reflection.[49] This implies that although the Fe_xO core is magnetic, the moments in the Fe_xO-core deviate from the [111] direction observed in bulk.[49] Remarkably, the refinement of the magnetic reflections unambiguously demonstrates that the core is AFM with the magnetic moments aligned along the [110] axis (Fig. 4a).

Magnetic measurements

The zero field cooled–field cooled (ZFC–FC) magnetization curves for the CS_9 sample (Fig. 5a) exhibit the characteristics of superparamagnetic systems[50] with a maximum in the ZFC magnetization, T_{max} = 90 K associated with the FiM Fe_3O_4-shell. This maximum is related to the blocking temperature (T_B) distribution due to the particle-size (or energy barrier) distribution. Notably, the ZFC–FC curves for the CS_45 particles (Fig. 5b) are markedly different. First, they do not merge at high temperatures, implying that the shell remains blocked (*i.e.*, FiM) at room temperature. Moreover, the kink at 120 K is attributed to the Verwey transition[51] of the Fe_3O_4-shell, *i.e.*, $T_V \sim 120$ K. The second feature at 240 K is attributed to the magnetic ordering of the Fe_xO core, *i.e.*, T_N = 240 K (somewhat larger than the bulk T_N of Fe_xO, $T_N \sim 200$ K[13,52]). Importantly, the enhancement of T_N with respect to the bulk values is supported by the temperature dependence of the intensity of the (1/2, 1/2, 1/2) magnetic reflection, which shows that the magnetic order of the Fe_xO core is maintained up to roughly $T_N \sim$ 240 K (Fig. 4b). To confirm that we are dealing with thermodynamic transitions and not blocking temperatures, we performed $M(T)$ measurements at different applied fields. As can be seen in the ESI Fig. S4† the T_V and T_N transition temperatures are virtually independent of the field, as expected. Shown in the insets of Fig. 5c, d are the hysteresis loops of the samples at 10 K after FC in 20 kOe from 300 K. The reduced saturation magnetization, M_S, values (obtained by subtracting the weight of the surfactant from the total mass), $M_S^{CS\_9}$ = 46 emu g^{-1} and $M_S^{CS\_45}$ = 52 emu g^{-1}, with respect to bulk magnetite (M_S = 90 emu g^{-1})[53] are in line with the presence of Fe_xO. The enlarged loops of both samples exhibit exchange bias (H_E) and increased coercivities (H_C), as expected from the AFM/FiM exchange coupling.[42] However, bearing in mind that, according to neutron diffraction, for the CS_9 particles the Fe_xO-core is not antiferromagnetically ordered, the observed H_E (~600 Oe) and H_C (~1000 Oe) should arise from other effects. For example, surface effects in metal oxide nanoparti-

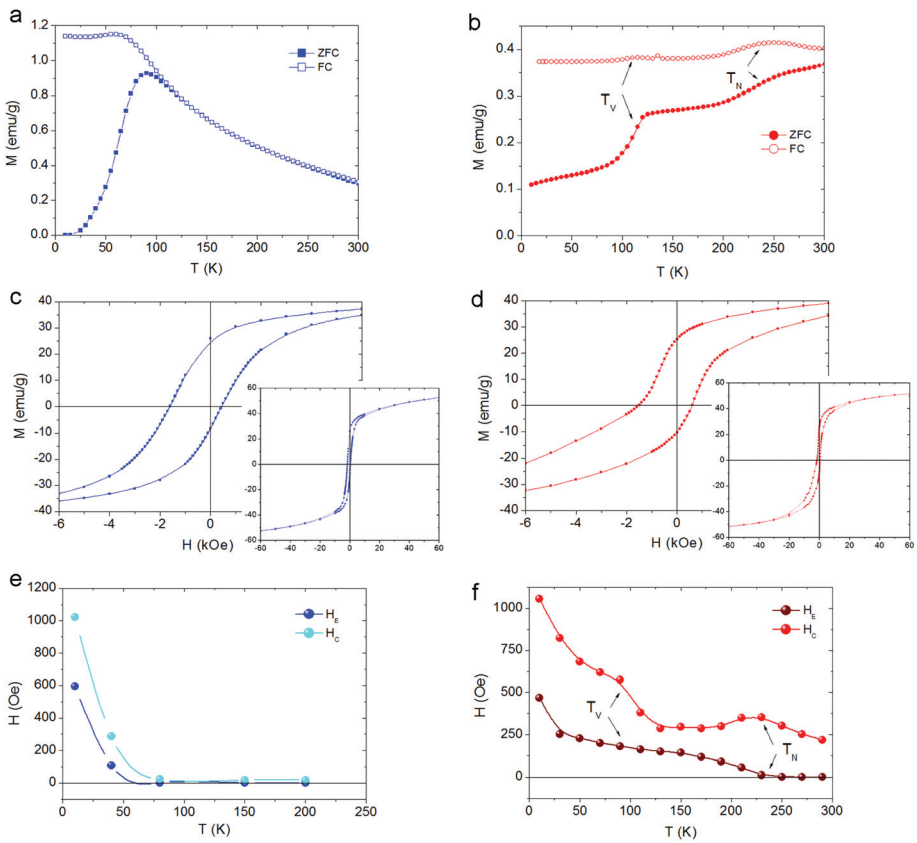

Fig. 5 Temperature dependence of the field cooled (FC) and zero field cooled (ZFC) magnetizations for (a) CS_9 and (b) CS_45 particles. Enlarged view at a low field of the hysteresis loops at 10 K for (c) CS_9 and (d) CS_45 nanoparticles. The insets show the hysteresis loops in the full field range. Temperature dependence of the coercivity, H_C, and the loop shift, H_E, for (e) CS_9 and (f) CS_45 nanoparticles. The lines are guides to the eye.

cles are known to result in H_E and enhanced H_C.[54,55] However, the large H_E and H_C observed for CS_9 indicate that, even if the Fe_xO-core is non-magnetic, the uncompensated spins of the Fe_3O_4-shell at the Fe_xO/Fe_3O_4 interface may also contribute to the exchange bias properties. In fact, Monte Carlo simulations demonstrate that a core/shell nanoparticle with a paramagnetic (PM) core can have a rather large exchange bias (ESI Fig. S5†). The temperature dependence of H_E and H_C (Fig. 5e) show that both quantities decrease rather fast, vanishing below T_B. Thus, there is no indication of the presence of a Verwey or Néel transitions, which is again consistent with the non-magnetic character of the Fe_xO core. On the other hand, for the CS_45 particles the temperature dependence of both H_E and H_C exhibits a rather intricate behaviour (Fig. 5f). When decreasing T, at about 230 K, H_E starts to increase while H_C exhibits a maximum. These are well known effects of the onset of AFM/ferromagnetic (FM) exchange bias.[56,57] Hence, H_C(T) and H_E(T) also support the enhanced T_N of the core. As the temperature is lowered further, at about T = 120 K, H_C exhibits a steep increase while H_E shows a subtle change of a slope. These features can be linked to the changes in the magnetocrystalline anisotropy (both in the intensity and the easy axis direction[58]) associated with the Verwey transition. Indeed, the strong temperature dependence of H_C around T_V is corroborated by Monte Carlo simulations. When assuming the known strong temperature dependence of the anisotropy of Fe_3O_4 [58] for the shell anisotropy, K_{SH} (see the inset of ESI Fig. S6†), and a reorientation of the easy axis from (111) to (100), the simulations clearly show that while H_C has a rather steep change at T_V, H_E changes more smoothly (ESI Fig. S6†), in concordance with the experimental results (Fig. 5f). Finally, at very low temperatures there is an additional increase in H_C and H_E. This is probably related to the fraction of small Fe_3O_4 nanoparticles observed in CS_45 by XRD and TEM.

Ferromagnetic resonance

The CS_9 nanoparticles show, at room temperature, a single isotropic resonance line centered at the resonance field H_r = 8.49(4) kOe, with a peak-to-peak linewidth, ΔH_{pp} = 1.03(4) kOe, which grows smoothly up to ~2 kOe as the temperature decreases (Fig. 6c, e). The results are analogous to the ones measured in low anisotropy Fe_3O_4 nanoparticles[59–62] and show no evidence of either T_N of Fe_xO or a Verwey transition, in agreement with the temperature dependence of H_C (Fig. 5e), which is also featureless.

The large CS_45 nanoparticles show a very broad and asymmetric spectrum with a secondary peak located at lower fields (Fig. 6d). At room temperature ΔH_{pp} is 2.79(8) kOe. Notably, the expected linewidth at room temperature for random oriented single phase Fe_3O_4 nanoparticles with cubic magnetocrystalline anisotropy ($K_1 \sim -1 \times 10^5$ erg cm^{-3} and $M_S \sim 55$ emu g^{-1}) leads to $\Delta H_{pp} = 5/3(2\ K/M_S) \sim 1.1$ kOe.[58,59,63,64] This value is almost three times smaller than the value obtained for the CS_45 nanoparticles, which suggests the presence of other significant contributions besides magnetocrystalline anisotropy. In line with this, the simulated profiles

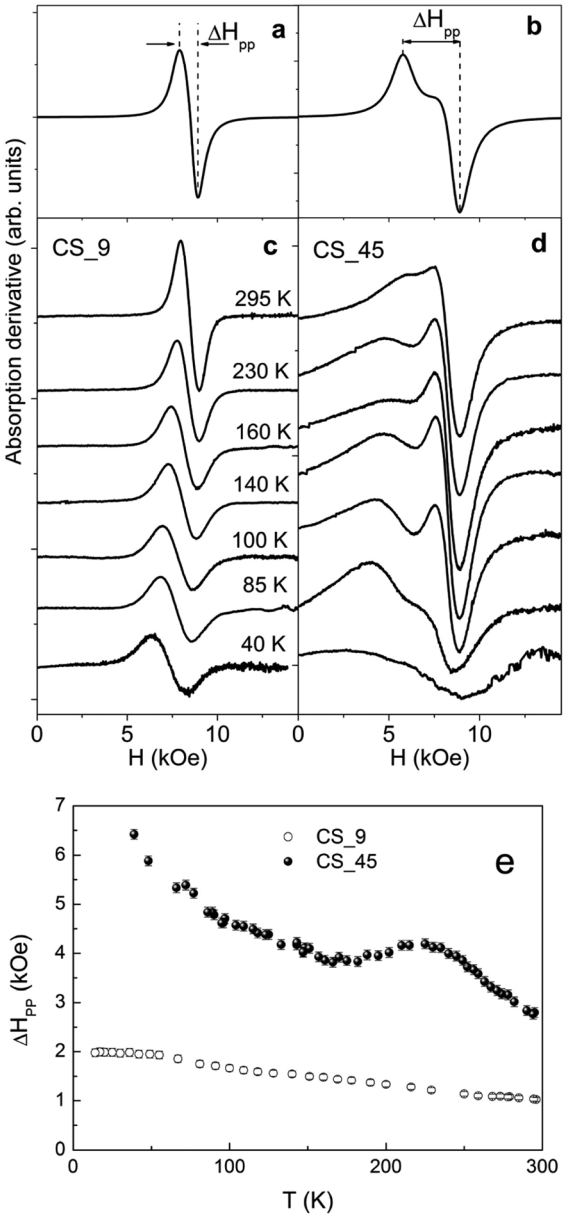

Fig. 6 Simulated ferromagnetic resonance (FMR) spectra using uniaxial effective anisotropies (a) $K_{eff} = 0.7 \times 10^5$ erg cm^{-3} (CS_9) and (b) $K_{eff} = 3.1 \times 10^5$ erg cm^{-3} (CS_45), respectively. FMR spectra measured at different temperatures for (c) CS_9 and (d) CS_45 nanoparticles, respectively. (e) Temperature dependence of the linewidth, ΔH_{pp}, for the CS_9 and CS_45 nanoparticles.

(Fig. 6a, b) confirm that the effective anisotropy of the large particles is considerably enhanced with respect to the small ones (see ESI† for details on the simulation parameters).

As can be seen in Fig. 6e, in contrast to the CS_9 particles, the temperature dependence of the FMR linewidth for CS_45 particles exhibits a markedly non-monotonic behavior. Namely, ΔH_{pp} has a peak at around $T \sim 230$ K. At about $T \sim 150$ K ΔH_{pp} increases moderately again. Finally, at low T there is a rather sharp increase in ΔH_{pp}. The peak in ΔH_{pp} at 230 K can be correlated with the increases in anisotropy expected in

AFM/FM systems at the AFM T_N,[56] and is consistent with $H_C(T)$ (Fig. 5f). Further, $\Delta H_{pp}(T)$ once again confirms the enhanced T_N of the Fe_xO core. Similarly, the upturn in ΔH_{pp} of CS_45 at moderate temperatures can be correlated with the evolution of the system to a phase of lower crystalline symmetry at T_V, consistent with the H_C behavior. However, a more direct correlation between the line shape and the anisotropy constants is rather difficult since (i) bulk Fe_3O_4 presents a complex temperature evolution of the magnetocrystalline contribution (*i.e.* due to a change in the crystal symmetry, from cubic to monoclinic, and the easy axis reorientation at T_V),[58] (ii) we are dealing with nanoparticle systems with a distribution of anisotropy constants arising from the particle size distribution, different degrees of crystallinity and magnetic disorder, and (iii) the particular morphology of the core/shell system can induce additional anisotropy terms like AFM/FiM exchange coupling, surface, shape or strain anisotropy.

Mössbauer spectroscopy

Mössbauer spectra for the CS_9 and CS_45 samples at different temperatures from 20 K to 300 K are shown in Fig. 7 and 8. The 300 K spectrum of the CS_9 (9 nm) particles (Fig. 7a) shows only a broad peak centered at 0.44 mm s^{-1}, while the spectrum of the CS_45 particles (45 nm) at the same temperature (Fig. 8a) shows well resolved sextets in addition to a central peak at around 1.0 mm s^{-1}.

For CS_9 while the spectrum in Fig. 7a is typical of superparamagnetic Fe-oxide nanoparticles, a small fraction of paramagnetic Fe_xO (less than 10%) cannot be completely ruled out (although, this value is considerably smaller than the 40% observed for CS_9 from EELS, XRD or neutrons). At 150 K (Fig. 7c) resolved Zeeman sextets start to appear. The spectra measured at 20 K and at 100 K (Fig. 7e, d), *i.e.*, below the Verwey temperature of bulk magnetite, were fitted using five components for Fe_3O_4, in agreement with other studies and indicate the presence of only Fe_3O_4 (see ESI†), without a clear evidence of Fe_xO in the sample.[65–67] For this sample, Mössbauer spectroscopy suggests a blocking temperature T_B close to 180 K, although some magnetic relaxation is still present at 100 K, as can be seen from the significant broadening of the spectral lines when compared to the spectrum at 20 K. The difference of T_B between Mössbauer and magnetometry stems from the difference in the characteristic measuring times between both techniques.[68] The obtained Mössbauer parameters of the fitting for the 20 K CS_9 spectrum are shown in Table S2 in ESI.†

For the CS_45 particles, the fit of the T = 300 K spectrum (Fig. 8a) allows the clear identification of Fe_3O_4 (ferrimagnetic at room temperature) as the main component (see ESI†). Moreover, the spectrum shows a broad paramagnetic central peak, with an isomer shift of 1.04(2) mm s^{-1} (20% of the spectral area), which can be assigned to paramagnetic Fe_xO (*i.e.*, above T_N). Although the Mössbauer spectrum of non-stoichiometric Fe_xO at room temperature typically consists of a sum of singlets and doublets, depending strongly on the defect concentration in the lattice (where different fitting methods have been applied to describe it[69–72]), due to the low resolution of the spectrum (broad velocity range, ±12 mm s^{-1}) and lines superposition, the 300 K Fe_xO peak was fitted to just one doublet (ESI Table S2†). A comparison of these Mössbauer parameters with weighted average values from ref. 75 and 77 suggests $x > 0.95$ for the Fe_xO core, in agreement with EELS and X-ray results. The fitting results at T = 300 K indicate about 20% of Fe_xO in the CS_45 particles, consistent also with the X-ray fits (ESI Table S2†). The spectra measured at 20 K and at 100 K, *i.e.*, below the Verwey temperature of bulk magnetite, were fitted using five components for Fe_3O_4. Thus, the fact that a higher number of sextets are needed to fit the low temperature spectra (with respect to high temperatures) clearly indicates a Verwey transition. As shown in Table S2,† the obtained Mössbauer parameters are in reasonable agreement with previous studies on magnetite.[66,67,73–77] Concerning the Fe_xO subspectrum, it can be seen that at low temperatures (≤150 K, Fig. 8b–d) the high temperature paramagnetic peak opens into a resolved complex spectrum, indicating that the

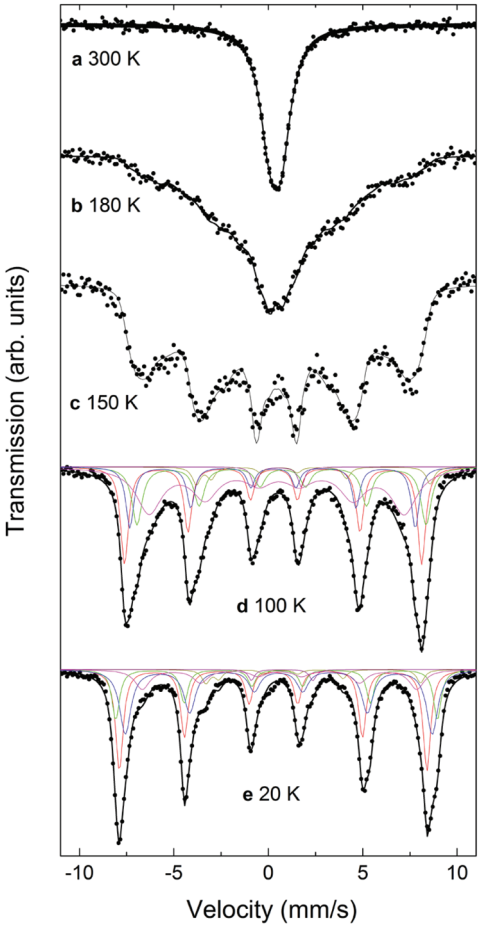

Fig. 7 Mössbauer spectra for the CS_9 particles at (a) 300 K, (b) 180 K, (c) 150 K, (d) 100 K, and (e) 20 K. Note that the fact that a fit with only two discrete sextets for Fe_3O_4 did not lead to satisfactory results can be interpreted as a clear evidence of the charge ordering in the CS_9 particles at these temperatures, although no Verwey transition can be identified.

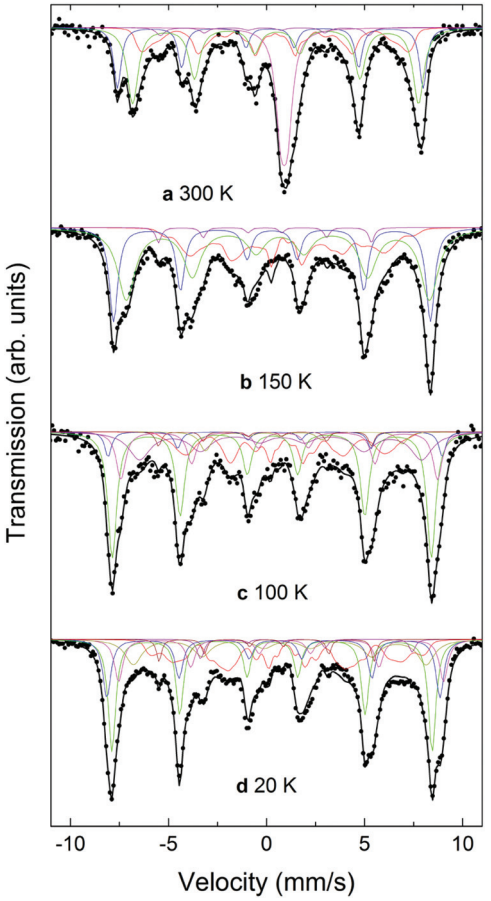

Fig. 8 Mössbauer spectra for the CS_45 particles at (a) 300 K, (b) 150 K, (c) 100 K, and (d) 20 K. The characteristics of the two resolved sextets correspond to Fe^{3+} in the tetrahedral (A) sites (the outermost sextet, 20%), and to Fe^{2+} and Fe^{3+} in the octahedral [B] sites (36%).

Fe_xO core becomes magnetic. However, the complexity of the Fe_xO spectrum (which in the fit is taken into account by an additional B_{HF} distribution), hinders obtaining accurate magnetostructural details. The resulting magnetic hyperfine field distribution (ESI Table S2†) is fully consistent with an antiferromagnetic Fe_xO core.[35,72] Additionally, Mössbauer spectroscopy indicates an ordering transition (*i.e.*, T_N) close to 220 K (ESI Fig. S7†) for this phase, in agreement with the neutron, ferromagnetic resonance and magnetometry results.

Discussion

Some of the contrasting properties observed in the two types of nanoparticles stem from different factors, including: (i) size effects, (ii) the exact stoichiometry of the Fe_xO core and (iii) the strains related to the core/shell structure. It is well known that as the size is reduced a number of effects occur in magnetic nanoparticles such as superparamagnetism or reduction of the transition temperatures.[50,78] Further, it is well established that in bulk the magnetic properties of Fe_xO are strongly dependent on the exact stoichiometry of Fe_xO.[79,80] Finally, another important aspect to be taken into account is the lattice mismatch between the core and the shell counterparts, which can induce significant strains (compressive or tensile) on both the core and the shell,[25] which can affect their physicochemical properties. This effect, combined with the strong dependence of the magnetic properties of Fe_xO on pressure,[48,77,81,82] can help to understand some of the properties.

The enhanced T_N with respect to bulk values observed in the large particles can be certainly explained from the combined effects of non-stoichiometry, x, and the internal pressure induced by the Fe_3O_4 shell. Notably, in bulk it has been shown that T_N depends strongly on x,[80,83,84] where the less stoichiometric samples have a larger T_N. Thus, from the estimation of x in the core/shell nanoparticles, obtained from the EELS analysis, $x \sim 0.95$, a higher T_N than in bulk is indeed plausible. However, $T_N \sim 240$ K is probably exceedingly large to be explained solely by non-stoichiometry. Additionally, neutron diffraction and Mössbauer studies have established that the T_N of Fe_xO increases with pressure for moderate pressures.[81,85] Since the lattice parameter of Fe_3O_4 is smaller than twice the one of Fe_xO, the lattice mismatch at the core/shell interface generates a compressive strain on the Fe_xO core, as indicated by the GPA analysis. Consequently, the large T_N observed experimentally is probably also influenced by the internal pressure, as observed previously in MnO/Mn_3O_4 core/shell particles,[47,86] although proximity effects due to the Fe_3O_4 shell cannot be ruled out.[87,88] However, it is difficult to determine the relative importance of the effects of stoichiometry and strains (and proximity effects) on T_N.

An additional novel effect observed in the large particles is that the magnetic moments of the Fe ions in the Fe_xO core are aligned along the [110] and not along the [111] direction as in the bulk phase.[49] This effect may again be related to both stoichiometry and strains. Theoretical calculations have shown that although the [111] direction appears to be an easy axis for Fe_xO, small changes (*e.g.*, trigonal asymmetries or deviations of the orbital moments) may change the easy axis to the (111) plane.[89–91] This implies that perturbations from the ideal Fe_xO structure may affect the effective easy axis of the system. Experimentally, in bulk it has been observed that the easy axis can significantly deviate from the [111] direction.[91–93] It has been argued that this deviation is related to a different magnetic ordering around the defects caused by non-stoichiometry,[91,93] which is in the (111) plane.[94] As the non-stoichiometry increases, the number of defect clusters grows, a higher tendency to (111) plane orientation of the moments would increase. Given that in the CS_45 samples we have $x \sim 0.95$, a reorientation of the easy axis is conceivable. Moreover, it has been theoretically predicted that a compressive strain could reorient the magnetic moments from [111] to the (111) plane due to orbital moments.[89] Therefore, the internal pressure observed in the deformation maps obtained by GPA is potentially also contributing to the observed easy axis reorientation. Interestingly, for CoO epitaxial thin films (with a similar spin structure) and Co/CoO core/shell nanoparticles it

has been demonstrated that the epitaxial strain can induce reorientations of the easy axis,[95,96] similar to the ones observed in the Fe_xO/Fe_3O_4 nanoparticles. Therefore, once again the combination of stoichiometry and strains appears to control the magnetic properties of the Fe_xO core. However, magnetic effects like perpendicular coupling and easy axis reorientation in FM/AFM systems[97–99] may also contribute to the observed [110] easy axis (*i.e.*, in the (111) plane).

Another appealing effect observed in the large particles is the bulk-like Verwey transition[51] of the Fe_3O_4 shell, $T_V \sim 120$ K, since it has been shown that in nanoparticles T_V is significantly affected by size effects. For example, nanoparticles in the range of 20–50 nm already show depleted T_V transitions[100,101] and smaller particles usually show no signs of T_V.[102] Although our nanoparticles with ~40 nm are at the high end of the size effects, it should be taken into account that Fe_3O_4 comprises only the shell with a rather reduced thickness (~9 nm). Hence, size effects would be somewhat expected. Moreover, T_V is also affected by stoichiometry and small deviations from Fe_3O_4 quickly suppress the transition.[103] Thus, the rather sharp Verwey transition at ~120 K shows an excellent stoichiometry of the Fe_3O_4 shell in concordance with EELS and XRD results. In the case of T_V, it is known that the pressure (*i.e.*, compressive stress) quickly decreases the transition temperature. However, since the lattice parameter of Fe_3O_4 is smaller than twice the one of Fe_xO, a tensile stress is expected in the shell from the core (opposing the compressive strain on the Fe_xO core). Thus, perhaps the tensile epitaxial strain favours the stability of the low temperature phase. Another factor to take into account is that the particles are rather cubic in shape and are consequently less prone to magnetic and structural surface effects which may influence T_V.[54,104]

Concerning the small particles, their $M(T)$ shows the typical shape of a superparamagnetic transition, indicating that due to their small size and moderate anisotropy, K, the anisotropy energy, KV, is rather low leading to a superparamagnetic behaviour.[50,78,102] However, the most striking feature of these particles is that, while structurally the presence of Fe_xO is confirmed by XRD and neutron diffraction, magnetically (magnetometry, neutron diffraction, FMR and Mössbauer) there is no clear sign of Fe_xO, except for the presence of an exchange bias. The first idea would be to relate the absence of a magnetic signal of Fe_xO to size effects. It is well known that the T_N in AFM nanoparticles is substantially reduced for small enough particles.[105–108] However, although this could explain the neutron diffraction results, a paramagnetic Fe_xO would lead to an unsplitted central peak in the Mössbauer spectrum,[77] as observed for the CS_45 particles at 300 K, which is virtually absent in our data. The large non-stoichiometry of the small particles suggests another origin for the observed effects. The cation deficiency in the Fe_xO structure leads to defects. Interestingly, in Fe_xO these defects tend to cluster forming in some cases Fe_3O_4-like structures.[109] These defect structures should have Mössbauer signatures similar to the Fe_3O_4 shell, since Mössbauer measures the short-range magnetic order rather than the long-range order measured by neutron diffraction. Consequently, a larger non-stoichiometry should lead to higher number of defects and hence weaker Fe_xO signs in the Mössbauer spectrum. In particular, the progressive oxidation of Fe_xO takes place by oxidizing the Fe^{2+} ions into Fe^{3+} ions. This should lead to the progressive appearance of higher magnetic hyperfine field components (absent in nearly stoichiometric Fe_xO) in the Mössbauer spectrum, similar to Fe_3O_4, as x decreases.[69,77] Nevertheless, in line with the large particles, another effect to take into account is pressure, particularly since the small particles probably have larger strains than the larger particles, as evidenced by their smaller lattice parameters. Although the effect of pressure on the magnetic properties of bulk Fe_xO is somewhat controversial,[77,81,110] it has been shown that the Mössbauer spectra tend to develop high hyperfine field components as the pressure is increased,[77,110] probably due to the fact that the defect clusters start approaching each other. This would contribute to the overlapping of the Fe_xO and Fe_3O_4 Mössbauer components, and a small fraction of Fe_xO could be "hidden" in the 20 K CS_9 spectrum. Thus, similar to non-stoichiometry the strain effects should also tend to decrease the typical features of Fe_xO in the Mössbauer spectra for the small particles. The combination of neutrons and Mössbauer seems to indicate that the Fe_xO is not magnetic (due to size effects) and that any Mössbauer signal arising from the core is a sign of local magnetism of the defect clusters rather than a true long range magnetic order of Fe_xO.[111] Notably, the presence of a sizable exchange bias can be explained without the need of an AFM counterpart. Although it is known that surface effects can give rise to an exchange bias,[54] Monte Carlo simulations indicate that the presence of a core/shell interface (even when the core is paramagnetic) can also contribute significantly to the exchange bias properties (ESI Fig. S5†). This exchange bias is in a sense similar to the exchange bias observed in hollow γ-Fe_2O_3 nanoparticles,[112] although in Fe_xO/Fe_3O_4 the interphase is probably magnetically less disordered than the inner shell in hollow structures.

Finally, note that in the small particles T_V of the Fe_3O_4 shell is lacking. Given the rather small size of the particles, this is probably due to the finite size effects.[78]

Conclusions

In summary, we have shown that the combination of diverse factors (*i.e.*, non-stoichiometry, core/shell strains and size effects) can shed some light on the broad range of properties exhibited by transition metal oxides at the nanoscale. Importantly, to clarify all these effects, a detailed, multi-technique, characterization is usually required. In particular, we have performed an exhaustive magneto-structural investigation of the smallest and largest Fe_xO/Fe_3O_4 core/shell nanoparticles (9 nm and 45 nm) reported in the literature. The results reveal a highly non-stoichiometric Fe_xO phase ($x \sim 0.80$) for the smaller particles which leads to the non-magnetic character of the Fe_xO core. On the other hand, the larger ones, with $x \sim$

0.95, exhibit an antiferromagnetic behaviour. Commonly, in transition metal oxides x depends on the synthesis and post-synthesis conditions as well as on the size, since smaller particles are more reactive thus more prone to oxidation and the reduced number of atoms in the particles implies a higher difficulty to reach a long-range crystal order. Similarly, the internal pressure is determined by several factors like the overall size of the particles, the thickness of the shell, the diameter of the core and shape. Furthermore, in the case of the Fe_xO phase since the lattice parameter depends significantly on x, the strain caused by the lattice mismatch will also depend on x. Hence, our results establish that although some of the overall properties of the Fe_xO/Fe_3O_4 nanoparticles can be similar (*e.g.*, the presence of an exchange bias or reduced magnetization), the exact features (the presence of T_V, enhanced T_N, or non-monotonic H_E and H_C dependence) will depend on the exact structure (*e.g.*, stoichiometry and internal strains) and morphology of the samples (*e.g.*, size or shape).

Methods

Synthesis of Fe_xO/Fe_3O_4 core/shell nanoparticles

All starting materials were purchased from Sigma-Aldrich, except oleic acid (99% of purity) that was acquired from TCI, and used without further purification. In the first step, the iron(III) oleate precursor was synthesized following the procedure described by Park *et al.*[113]

The small nanoparticles (CS_9) were obtained by dissolving 2 g (1.95 mmol) of iron(III) oleate and 0.09 g (0.32 mmol) of oleic acid in 20 mL of 1-octadecene. The reaction system was degassed at 100 °C under magnetic stirring by carrying out cycles of vacuum/argon. Subsequently, the mixture was heated up to 320 °C (at 7–8 °C min^{-1}) in argon and kept for 30 min.

To synthesize the larger nanoparticles (CS_45), the previous method was slightly modified according to the procedure proposed by Wetterskog *et al.*[25] Namely, 10.25 g (10 mmol) of iron(III) oleate were dissolved in 34 mL of eicosane together with 1.44 g (5.12 mmol) of oleic acid and 1.56 g (5.12 mmol) of sodium oleate. After being degassed under a nitrogen atmosphere, the solution was heated at 100 °C for 2 h to dissolve the sodium oleate. The temperature was then increased to 350 °C using a 3 °C min^{-1} heating rate. The mixture was maintained at this temperature for 30 min. For both systems the slurry was exposed to air after removing it from the heating source and allowed to cool down to room temperature. The nanoparticles were washed by several cycles of coagulation with ethanol, centrifugation at 2000g, disposal of supernatant solution and re-dispersion in hexane and n-heptane for CS_9 and CS_45, respectively.

Structural and morphological characterization

Transmission electron microscopy (TEM) images were obtained using a Jeol JEM-2100 with a LaB_6 filament. High-angle annular dark-field (HAADF) imaging and electron energy loss spectra (EELS) were collected using a Jeol J2010F (S)TEM operating at 200 kV and coupled to a GIF spectrometer and in an FEI Titan operated at 80 kV fitted with a CEOS Probe Corrector and a Gatan Tridiem Energy Filter. EEL data were acquired at about every 1 nm along the diameter of the nanoparticles at an energy range containing the Fe–$L_{2,3}$ and O–K edges with an energy resolution of 0.8 eV. Fe/O quantification was performed using Gatan Digital Micrograph commercial software. The Fe oxidation state was obtained from a homemade script ("Oxide Wizard") for Gatan Digital Micrograph software,[8] where the required iron oxide reference data were obtained from Schmid *et al.*[114] X-ray diffraction patterns were collected at 300 K at the ID31 beamline of the European Synchrotron Radiation Facility (ESRF) with a wavelength of 0.4 Å for the CS_9 particles and at the BL04-MSPD of the ALBA Synchrotron Light Facility with a wavelength of 0.62 Å for the CS_45 sample.

Geometric phase analysis

The geometric phase analysis (GPA) was carried out using the GPA plugin by HREM Research Inc. In this case, *e.g.*, a 1D case (deformation mapping), only one spot corresponding to a given crystallographic interplanar spacing was chosen (see ESI Fig. S1†). Details of the analysis can be found in ref. 25.

In the GPA analysis a cosine mask was used on $\mathbf{g}_{200(\text{wüstite})}$/$\mathbf{g}_{400(\text{spinel})}$ and $\mathbf{g}_{220(\text{spinel})}$, where the size of the mask corresponded to a resolution of 0.9 nm and 1.2 nm, respectively. The width of the integration profiles shown in Fig. 3 was chosen to match the lateral resolution of the images.

Neutron diffraction

Neutron diffraction measurements were carried out at 10 K using a D20 diffractometer of the Institute Laue-Langevin with a neutron wavelength of 1.5 Å for the CS_9 particles and in the temperature range from 15 to 270 K both using the 6T2 and G61 diffractometers of the Laboratoire Léon Brillouin with a neutron wavelength of 2.34 and 4.74 Å, respectively, for the CS_45 sample. All diffraction patterns were analyzed using FullProf[115] based on the known crystal and magnetic structures of Fe_xO and Fe_3O_4.

Magnetic measurements

The magnetic properties were measured on tightly packed powdered samples using a superconducting quantum interference device (SQUID, Quantum Design) magnetometer with a 70 kOe maximum field. The measurements of the temperature dependence of magnetization, $M(T)$, were carried out at 20 Oe after either zero field cooling (ZFC) or field cooling (FC) in 20 Oe from 300 K to 10 K. Some $M(T)$ measurements were also carried out at different applied fields (200 and 2000 Oe). Hysteresis loops, $M(H)$, were obtained after FC in 20 kOe from 300 to 10 K. The loops were obtained sequentially at increasing fixed temperatures.

Ferromagnetic resonance measurements

Ferromagnetic resonance spectra were recorded with a commercial Bruker ESP300 spectrometer at a frequency of ν = 24 GHz (K-band) in the 5–300 K temperature range.

Mössbauer measurements

Transmission ^{57}Fe Mössbauer spectroscopy measurements were conducted at different temperatures ranging from 20 to 300 K, using a closed cycle cryostat, a conventional constant acceleration transducer and a ^{57}Co/Rh source. The Normos least-squares fit program[116] was employed for data evaluation and identical recoil-free fractions were assumed for all phases and lattice sites. The isomer shift values are quoted relative to α-Fe at room temperature.

Monte Carlo simulations

To model the large particles, CS_45, we consider cubic nanoparticles on a simple cubic (sc) lattice, consisting of an AFM core with an edge length (L_C = 12) and a FiM shell (t_{SH} = 3), surrounding the core. The spins in the particles interact with the nearest neighbour's Heisenberg exchange interaction, and at each crystal site they experience a uniaxial anisotropy. In the presence of an external magnetic field, the total energy of the system is

$$H = -J_C \sum_{i,j\in \text{core}} \vec{S}_i \cdot \vec{S}_j - J_{SH} \sum_{i,j\in \text{shell}} \vec{S}_i \cdot \vec{S}_j - J_{IF} \sum_{i\in \text{core}, j\in \text{shell}} \vec{S}_i \cdot \vec{S}_j - K_C \sum_{i\in \text{core}} \left(\vec{S}_i \cdot \hat{e}_i\right)^2 - K_{SH} \sum_{i\in \text{shell}} \left(\vec{S}_i \cdot \hat{e}_i\right)^2 - \vec{H} \cdot \sum_i \vec{S}_i \quad (1)$$

Here S_i is the atomic spin at site i and $\hat{e}_i$ is the unit vector in the direction of the easy axis at site i. We consider the magnitude of the atomic spins in the two AFM sublattices equal to 1 and in the two FiM sublattices of the shell to be equal to 1 and 1.5, respectively. The first term in eqn (1) gives the exchange interaction between the spins in the AFM core; the second term gives the exchange interaction between the spins in the FiM shell. We consider the exchange coupling constant of the core as $J_C = -0.5J_{FM}$ and that of the shell as $J_{SH} = -1.5J_{FM}$, where J_{FM} is considered to be the exchange coupling constant of a pure ferromagnet (FM), J_{FM} = 1 is taken as the reference value. The third term gives the exchange interaction at the interface between the core and the shell. The interface includes the last layer of the AFM core and the first layer of the FiM shell. The exchange coupling constant of the interface J_{IF} is taken to be equal to that of the shell J_{SH}. The fourth term gives the anisotropy energy of the AFM core, $K_C = 0.05J_{FM}$. Based on our neutron diffraction results, K_C is assumed to be along the [110] direction and constant in the whole temperature range studied. If the site i lies in the outer layer of the AFM core then $K_{iC} = K_{IF\_C}$, and $K_{iC} = K_C$ elsewhere. The core and the shell interface anisotropies are the same as the shell anisotropy for all temperatures. The fifth term gives the anisotropy energy of the FiM shell. To account for the strong non-monotonic temperature dependence of the K of Fe_3O_4 around the Verwey transition,[58] we have set a different K_{SH} value at each simulated temperature (see the inset in Fig. S6 in ESI†). If i lies in the outer layer of the shell (*i.e.*, the surface) then the anisotropy is taken to be random and smoothly changing with T from $K_S = 3.0J_{FM}$ ($T = 0.01J_{FM}/k_B$) to $1.6J_{FM}$ ($T = 0.5J_{FM}/k_B$). Importantly, based on the literature results for Fe_3O_4 around T_V,[51,58] two different directions are considered for the shell anisotropy, along the [100] direction for $T < T_V$ and along the [111] direction for $T > T_V$. Note that in concordance with the literature values, T_V is taken to be about 1/7 of the ferrimagnetic transition temperature of the shell ($T_C \sim 1.75J_{FM}/k_B$), *i.e.*, $T_V = 0.25J_{FM}/k_B$. Moreover, from the parameters used in the simulation the T_N of the core is established to be $T_N = 0.7J_{FM}/k_B$. The last term in eqn (1) is the Zeeman energy.

We performed our simulations on isolated, cubic (AFM) core/(FiM) shell nanoparticles using the MC simulation technique with the implementation of the Metropolis algorithm.[117] A hysteresis loop is calculated after a field cooling procedure starting at temperature $T = 2.0J_{FM}/k_B$ down to $T_f = 0.01J_{FM}/k_B$, at a constant rate under a static magnetic field $H_{cool} = 6.0J_{FM}/g\mu_B$. To account for the experimental random distribution of nanoparticles,[7] the cooling fields have been applied in different directions defined by spherical coordinates (θ,φ), where θ = 0, 15,..., 180 and φ = 0, 15,..., 345 degrees. The final hysteresis loop is calculated by averaging the hysteresis loops for each magnetic field direction according to the equation:

$$M = \frac{1}{4\pi}\int_0^{2\pi}\int_0^{\pi} M(\theta,\varphi)\sin\theta \mathrm{d}\theta\mathrm{d}\varphi \quad (2)$$

The hysteresis loop shift on the field axis gives the exchange field $H_E = -(H_{right} + H_{left})/2$. The coercive field is defined as $H_C = (H_{right} - H_{left})/2$. H_{right} and H_{left} are the points where the loop intersects the field axis. The fields H, H_C and H_E are given in dimensionless units of $J_{FM}/g\mu_B$, the temperature T in units J_{FM}/k_B and the anisotropy coupling constants K in units of J_{FM}. We have used 10^4 MC steps per spin (MCSS) at each field step and the results were averaged over 50–200 different samples (namely random numbers) depending on the fluctuations in the calculated values. The small nanoparticles, CS_9 are simulated using a spherical morphology with an FiM shell (t_{SH} = 3) and a core size of three lattice spacings in diameter (d_C = 3). The material parameters for the shell are the ones used above for the large particles at low T ($J_{SH} = J_{IF\_SH} = -1.5J_{FM}$, $K_{SH} = K_{IF\_SH} = 0.3$). The surface anisotropy is taken at random with $K_S = 3.0J_{FM}$. However, four different types of cores are considered in this case:

(1) AFM core with the same parameters as for CS_45, *i.e.*, $J_C = -0.5J_{FM}$, and $K_C = 0.05$.

(2) Paramagnetic core with $J_C = 0.00$, $K_C = 0.00$.

(3) FiM core with the same parameters as the shell (*i.e.*, a homogeneous FiM particle).

(4) No core (*i.e.*, a hollow nanoparticle).

Notably, the internal surface of the particle is also assumed to have a random anisotropy with the same K_S as the external surface. Since we are only interested in the trends, for simplicity, the anisotropy and magnetic fields are assumed to be along the z-axis, thus no angular hysteresis loop averaging is performed.

Acknowledgements

This work was supported by the 2014-SGR-1015 and 2009-SGR-35 projects of the Generalitat de Catalunya, by the MAT2010-20616-C02, MAT2011-27380-C02-01, MAT2010-16407, MAT2013-48628-R and CSD2009-00013 projects of the Spanish Ministerio de Economía y Competitividad (MINECO), the ONDA and COEFNANO projects (no. FP7-PEOPLE-2009-IRSES-247518 and no. FP7-PEOPLE-2012-IRSES-318901) of the European Union, the Russian grants RFBR 13-02-00121, 13-02-12429 and RG 14.B25.31.0025, the Brazilian grants CNPq-304368/2010-5 and FAPEMIG-PPM 00319-11, the Argentine grants PIP 1333 (CONICET) and SECTyP 06/C404 (Univ. Nac. de Cuyo) and the Swedish Research Council (VR). Research at NCSR "D" was supported by the HSF-EU program ARISTEIA, grant COMANA/22. GSA was partially supported by the Knut and Alice Wallenberg Foundation (Project: 3DEM-NATUR). I.V.G. thanks the Generalitat de Catalunya for his sabbatical fellowship (2010 PIV 00096). M.D.B. was partially supported by an ICREA Academia award. M.E. acknowledges the Spanish Ministry of Science and Innovation through the Juan de la Cierva Program. A. G. Roca would like to thank Generalitat de Catalunya for financial support under the Beatriu de Pinós fellowship program (2011 BP_B 00209). ICN2 acknowledges support from the Severo Ochoa Program (MINECO, grant SEV-2013-0295). We also acknowledge the European Synchrotron Radiation Facility (ESRF, Grenoble, France) and the ALBA Synchrotron Light Facility for the provision of synchrotron beam time and the Institute Laue-Langevin (ILL) and Laboratoire Léon Brillouin (LLB) for the provision of neutron beam time.

References

1 M. T. Greiner, L. Chai, M. G. Helander, W. M. Tang and Z.-H. Lu, *Adv. Funct. Mater.*, 2012, **22**, 4557–4568.
2 P. Poizot, S. Laruelle, S. Grugeon, L. Dupont and J. M. Tarascon, *Nature*, 2000, **407**, 496–499.
3 Y. Tokura, *Rep. Prog. Phys.*, 2006, **69**, 797–851.
4 G. S. Park, Y. B. Kim, S. Y. Park, X. S. Li, S. Heo, M. J. Lee, M. Chang, J. H. Kwon, M. Kim, U. I. Chung, R. Dittmann, R. Waser and K. Kim, *Nat. Commun.*, 2013, **4**, 2382.
5 A. Juhin, A. López-Ortega, M. Sikora, C. Carvallo, M. Estrader, S. Estradé, F. Peiró, M. D. Baró, P. Sainctavit, P. Glatzel and J. Nogués, *Nanoscale*, 2014, **6**, 11911–11920.
6 K. L. Krycka, J. A. Borchers, G. Salazar-Alvarez, A. López-Ortega, M. Estrader, S. Estradé, E. Winkler, R. D. Zysler, J. Sort, F. Peiró, M. D. Baró, C. Kao and J. Nogués, *ACS Nano*, 2013, **7**, 921–931.
7 A. López-Ortega, M. Estrader, G. Salazar-Alvarez, S. Estradé, I. V. Golosovsky, R. K. Dumas, D. J. Keavney, M. Vasilakaki, K. N. Trohidou, J. Sort, F. Peiró, S. Suriñach, M. D. Baró and J. Nogués, *Nanoscale*, 2012, **4**, 5138–5147.
8 L. Yedra, E. Xuriguera, M. Estrader, A. López-Ortega, M. D. Baró, J. Nogués, M. Roldan, M. Varela, S. Estradé and F. Peiró, *Microsc. Microanal.*, 2014, **20**, 698–705.
9 T. Zhang, X. P. Wang, Q. F. Fang and X. G. Li, *Appl. Phys. Rev.*, 2014, **1**, 031302.
10 F. X. Redl, C. T. Black, G. C. Papaefthymiou, R. L. Sandstrom, M. Yin, H. Zeng, C. B. Murray and S. P. O'Brien, *J. Am. Chem. Soc.*, 2004, **126**, 14583–14599.
11 S. Sun and H. Zeng, *J. Am. Chem. Soc.*, 2002, **124**, 8204–8205.
12 P. Guardia, A. Labarta and X. Batlle, *J. Phys. Chem. C*, 2011, **115**, 390–396.
13 R. Cornell and U. Schwertmann, *The Iron Oxides: Structure, Properties, Reactions, Occurences and Uses*, New York, 2nd edn, 2003.
14 P. Tartaj, M. P. Morales, T. Gonzalez-Carreño, S. Veintemillas-Verdaguer and C. J. Serna, *Adv. Mater.*, 2011, **23**, 5243–5249.
15 A. Glaria, M. L. Kahn, P. Lecante, B. Barbara and B. Chaudret, *ChemPhysChem*, 2008, **9**, 776–780.
16 H. Si, C. Zhou, H. Wang, S. Lou, S. Li, Z. Du and L. S. Li, *J. Colloid Interface Sci.*, 2008, **327**, 466–471.
17 M. Yin, Z. Chen, B. Deegan and S. O'Brien, *J. Mater. Res.*, 2011, **22**, 1987–1995.
18 Y. Hou, Z. Xu and S. Sun, *Angew. Chem., Int. Ed.*, 2007, **46**, 6329–6332.
19 L. M. Bronstein, X. Huang, J. Retrum, A. Schmucker, M. Pink, B. D. Stein and B. Dragnea, *Chem. Mater.*, 2007, **19**, 3624–3632.
20 H. T. Hai, H. T. Yang, H. Kura, D. Hasegawa, Y. Ogata, M. Takahashi and T. Ogawa, *J. Colloid Interface Sci.*, 2010, **346**, 37–42.
21 M. I. Bodnarchuk, M. V. Kovalenko, H. Groiss, R. Resel, M. Reissner, G. Hesser, R. T. Lechner, W. Steiner, F. Schäffler and W. Heiss, *Small*, 2009, **5**, 2247–2252.
22 D. W. Kavich, J. Dickerson, S. Mahajan, S. Hasan and J. H. Park, *Phys. Rev. B: Condens. Matter*, 2008, **78**, 174414.
23 C. J. Chen, R.-K. Chiang, H. Y. Lai and C. R. Lin, *J. Phys. Chem. C*, 2010, **114**, 4258–4263.
24 H. T. Hai, H. Kura, M. Takahashi and T. Ogawa, *J. Colloid Interface Sci.*, 2010, **341**, 194–199.
25 E. Wetterskog, C. Tai, J. Grins, L. Bergström and G. Salazar-Alvarez, *ACS Nano*, 2013, **7**, 7132–7144.
26 B. P. Pichon, O. Gerber, C. Lefevre, I. Florea, S. Fleutot, W. Baaziz, M. Pauly, M. Ohlmann, C. Ulhaq, O. Ersen, V. Pierron-Bohnes, P. Panissod, M. Drillon and S. Begin-Colin, *Chem. Mater.*, 2011, **23**, 2886–2900.
27 A. Lak, M. Kraken, F. Ludwig, A. Kornowski, D. Eberbeck, S. Sievers, F. J. Litterst, H. Weller and M. Schilling, *Nanoscale*, 2013, **5**, 12286–12295.
28 H. Khurshid, W. Li, S. Chandra, M.-H. Phan, G. C. Hadjipanayis, P. Mukherjee and H. Srikanth, *Nanoscale*, 2013, **5**, 7942–7952.
29 K. Simeonidis, S. Mourdikoudis, I. Tsiaoussis, N. Frangis, M. Angelakeris, O. Kalogirou, A. Delimitis and C. Dendrinou-Samara, *Mod. Phys. Lett. B*, 2007, **21**, 1143–1151.

30 A. Corrias, G. Mountjoy, D. Loche, V. Puntes, A. Falqui, M. Zanella, W. J. Parak and M. F. Casula, *J. Phys. Chem. C*, 2009, **113**, 18667–18675.
31 S. K. Sharma, J. M. Vargas, K. R. Pirota, S. Kumar, C. G. Lee and M. Knobel, *J. Alloys Compd.*, 2011, **509**, 6414–6417.
32 M. J. Benitez, D. Mishra, P. Szary, G. A. Badini Confalonieri, M. Feyen, A. H. Lu, L. Agudo, G. Eggeler, O. Petracic and H. Zabel, *J. Phys.: Condens. Matter*, 2011, **23**, 126003.
33 H. T. Hai, H. Kura, M. Takahashi and T. Ogawa, *J. Appl. Phys.*, 2010, **107**, 09E301.
34 R. Chalasani and S. Vasudevan, *J. Phys. Chem. C*, 2011, **115**, 18088–18093.
35 A. Lak, J. Dieckhoff, F. Ludwig, J. M. Scholtyssek, O. Goldmann, H. Lünsdorf, D. Eberbeck, A. Kornowski, M. Kraken, F. J. Litterst, K. Fiege, P. Mischnick and M. Schilling, *Nanoscale*, 2013, **5**, 11447–11455.
36 X. Sun, N. F. Huls, A. Sigdel and S. Sun, *Nano Lett.*, 2012, **12**, 246–251.
37 H. Khurshid, S. Chandra, W. Li, M. H. Phan, G. C. Hadjipanayis, P. Mukherjee and H. Srikanth, *J. Appl. Phys.*, 2013, **113**, 17B508.
38 A. Stamatiou, P. G. Loutzenhiser and A. Steinfeld, *Chem. Mater.*, 2010, **22**, 851–859.
39 L. Xiao, S. Y. Wu and Y.-R. Li, *Renewable Energy*, 2012, **41**, 1–12.
40 L. Shi, Y. D. He, X. H. Xia, Z. M. Jian and H. B. Liu, *J. Iran Chem. Soc.*, 2010, **7**, 721–726.
41 J. Zheng, Z. Yu, G. Ji, X. Lin, H. Lv and Y. Du, *J. Alloys Compd.*, 2014, **602**, 8–15.
42 J. Nogués, J. Sort, V. Langlais, V. Skumryev, S. Suriñach, J. S. Muñoz and M. D. Baró, *Phys. Rep.*, 2005, **422**, 65–117.
43 W. H. Meiklejohn and C. Bean, *Phys. Rev.*, 1956, **102**, 1413–1414.
44 J. Nogués, V. Skumryev, J. Sort, S. Stoyanov and D. Givord, *Phys. Rev. Lett.*, 2006, **97**, 157203.
45 G. Margaris, K. N. Trohidou and J. Nogués, *Adv. Mater.*, 2012, **24**, 4331–4336.
46 G. Salazar-Alvarez, J. Sort, S. Suriñach, M. D. Baro and J. Nogués, *J. Am. Chem. Soc.*, 2007, **129**, 9102–9108.
47 A. López-Ortega, D. Tobia, E. Winkler, I. V. Golosovsky, G. Salazar-Alvarez, S. Estradé, M. Estrader, J. Sort, M. A. González, S. Suriñach, J. Arbiol, F. Peiró, R. D. Zysler, M. D. Baró and J. Nogués, *J. Am. Chem. Soc.*, 2010, **132**, 9398–9407.
48 C. A. McCammon and L. Liu, *Phys. Chem. Miner.*, 1984, **10**, 106–113.
49 W. Roth, *Phys. Rev.*, 1958, **110**, 1333–1341.
50 M. Knobel, W. Nunes, L. Socolovsky, E. De Biasi, J. M. Vargas and J. Denardin, *J. Nanosci. Nanotechnol*, 2008, **8**, 2836–2857.
51 F. Walz, *J. Phys.: Condens. Matter*, 2002, **14**, R285–R340.
52 G. Srinivasan and M. S. Seehra, *Phys. Rev. B: Condens. Matter*, 1983, **28**, 6542–6544.
53 A. G. Roca, M. P. Morales, K. O'Grady and C. J. Serna, *Nanotechnology*, 2006, **17**, 2783–2788.
54 G. Salazar-Alvarez, J. Qin, V. Sepelák, I. Bergmann, M. Vasilakaki, K. N. Trohidou, J. D. Ardisson, W. A. A. Macedo, M. Mikhaylova, M. Muhammed, M. D. Baró and J. Nogués, *J. Am. Chem. Soc.*, 2008, **130**, 13234–13239.
55 N. Rinaldi-Montes, P. Gorria, D. Martínez-Blanco, A. B. Fuertes, L. Fernández Barquín, J. Rodríguez Fernández, I. de Pedro, M. L. Fdez-Gubieda, J. Alonso, L. Olivi, G. Aquilanti and J. A. Blanco, *Nanoscale*, 2014, **6**, 457–465.
56 J. Nogués and I. K. Schuller, *J. Magn. Magn. Mater.*, 1999, **192**, 203–232.
57 C. Leighton, M. Fitzsimmons, A. Hoffmann, J. Dura, C. F. Majkrzak, M. S. Lund and I. K. Schuller, *Phys. Rev. B: Condens. Matter*, 2002, **65**, 064403.
58 S. Chikazumi, in AIP Conf. Proc., AIP, 1976, vol. 29, pp. 382–387.
59 N. Guskos, E. A. Anagnostakis, V. Likodimos, T. Bodziony, J. Typek, M. Maryniak, U. Narkiewicz, I. Kucharewicz and S. Waplak, *J. Appl. Phys.*, 2005, **97**, 024304.
60 E. De Biasi, E. Lima, C. A. Ramos, A. Butera and R. D. Zysler, *J. Magn. Magn. Mater.*, 2013, **326**, 138–146.
61 S. Pal, P. Dutta, N. Shah, G. P. Huffman and M. S. Seehra, *IEEE Trans. Magn.*, 2007, **43**, 3091–3093.
62 Y. Köseoglu and H. Kavas, *J. Nanosci. Nanotechnol.*, 2008, **8**, 584–590.
63 E. Lima, A. L. Brandl, A. D. Arelaro and G. F. Goya, *J. Appl. Phys.*, 2006, **99**, 083908.
64 A. H. Morrish, *The Physical Principles of Magnetism*, New York, NY, 2001.
65 R. S. Hargrove and W. Kündig, *Solid State Commun.*, 1970, **8**, 303–308.
66 F. J. Berry, S. Skinner and M. F. Thomas, *J. Phys.: Condens. Matter*, 1998, **10**, 215–220.
67 A. G. Roca, J. F. Marco, M. P. Morales and C. J. Serna, *J. Phys. Chem. C*, 2007, **111**, 18577–18584.
68 M. Popovici, M. Gich, A. Roig, L. Casas, E. Molins, C. Savii, D. Becherescu, J. Sort, S. Suriñach, J. S. Muñoz, M. D. Baró and J. Nogués, *Langmuir*, 2004, **20**, 1425–1429.
69 N. N. Greenwood and A. T. Howe, *J. Chem. Soc., Dalton Trans.*, 1972, 110–116.
70 C. Wilkinson, A. K. Cheetham, G. J. Long, P. D. Battle and D. A. O. Hope, *Inorg. Chem.*, 1984, **23**, 3136–3141.
71 T. Yoshikawa, Y. Kanke, H. Yanagihara, E. Kita, Y. Tsunoda, K. Siratori and K. Kohn, *Hyperfine Interact.*, 2012, **205**, 135–138.
72 C. A. McCammon and D. C. Price, *Phys. Chem. Miner.*, 1985, **11**, 250–254.
73 I. Dézsi, C. Fetzer, A. Gombkötő, I. Szűcs, J. Gubicza and T. Ungár, *J. Appl. Phys.*, 2008, **103**, 104312.
74 T. J. Daou, G. Pourroy, S. Bégin-Colin, J. M. Grenèche, C. Ulhaq-Bouillet, P. Legaré, P. Bernhardt, C. Leuvrey and G. Rogez, *Chem. Mater.*, 2006, **18**, 4399–4404.
75 A. C. Doriguetto, N. G. Fernandes, A. I. C. Persiano, E. N. Filho, J. M. Grenèche and J. D. Fabris, *Phys. Chem. Miner.*, 2003, **30**, 249–255.

76 N. A. Fellenz, L. A. Cano, J. F. Bengoa, I. de Souza Azevedo, R. C. Mercader and S. G. Marchetti, *Hyperfine Interact.*, 2011, **202**, 17–24.
77 S. Nasu, *Hyperfine Interact.*, 1994, **90**, 59–75.
78 X. Batlle and A. Labarta, *J. Phys. D: Appl. Phys.*, 2002, **35**, R15–R42.
79 R. M. Hazen and R. Jeanloz, *Rev. Geophys.*, 1984, **22**, 37–46.
80 F. B. Koch and M. E. Fine, *J. Appl. Phys.*, 1967, **38**, 1470–1471.
81 I. Kantor, L. Dubrovinsky, C. Mccammon, N. Dubrovinskaia, I. Goncharenko, A. Kantor, A. Kuznetsov and W. Crichton, *Phase Transitions*, 2007, **80**, 1151–1163.
82 S. V. Ovsyannikov, V. V. Shchennikov, M. A. Shvetsova, L. S. Dubrovinsky and A. Polian, *Phys. Rev. B: Condens. Matter*, 2010, **81**, 060101.
83 M. S. Seehra and G. Srinivasan, *J. Phys. C: Solid State Phys.*, 1984, **17**, 883–892.
84 A. Pattek-Janczyk, B. Sepioł, J. C. Grenier and L. Fournès, *Mater Res. Bull.*, 1986, **21**, 1083–1092.
85 K. Glazyrin, L. Dubrovinsky, S. Klotz, M. Uhlarz, J. Wosnitza, T. Hansen and N. Dubrovinskaia, *J. Appl. Phys.*, 2011, **110**, 026109.
86 N. J. O. Silva, M. Karmaoui, V. S. Amaral, I. Puente-Orench, J. Campo, I. da Silva, A. Ibarra, R. Bustamante, A. Millán and F. Palacio, *Phys. Rev. B: Condens. Matter*, 2013, **87**, 224429.
87 I. V. Golosovsky, G. Salazar-Alvarez, A. López-Ortega, M. González, J. Sort, M. Estrader, S. Suriñach, M. Baró and J. Nogués, *Phys. Rev. Lett.*, 2009, **102**, 247201.
88 P. K. Manna and S. M. Yusuf, *Phys. Rep.*, 2014, **535**, 61–99.
89 I. V. Solovyev, A. I. Liechtenstein and K. Terakura, *J. Magn. Magn. Mater.*, 1998, **185**, 118–120.
90 A. Schrön and F. Bechstedt, *J. Phys.: Condens. Matter*, 2013, **25**, 486002.
91 H. Fjellvåg, F. Grønvold, S. Stølen and B. Hauback, *J. Solid State Chem.*, 1996, **124**, 52–57.
92 H. Fjellvåg, B. C. Hauback, T. Vogt and S. Stølen, *Am. Mineral*, 2002, **87**, 347–349.
93 P. J. Saines, M. G. Tucker, D. A. Keen, A. K. Cheetham and A. L. Goodwin, *Phys. Rev. B: Condens. Matter*, 2013, **88**, 134418.
94 P. D. Battle and A. K. Cheetham, *J. Phys. C: Solid State Phys.*, 1979, **12**, 337–345.
95 S. Csiszar, M. Haverkort, Z. Hu, A. Tanaka, H. Hsieh, H. J. Lin, C. Chen, T. Hibma and L. Tjeng, *Phys. Rev. Lett.*, 2005, **95**, 187205.
96 S. Inderhees, J. Borchers, K. Green, M. Kim, K. Sun, G. Strycker and M. Aronson, *Phys. Rev. Lett.*, 2008, **101**, 117202.
97 E. Jiménez, J. Camarero, J. Sort, J. Nogués, N. Mikuszeit, J. García-Martín, A. Hoffmann, B. Dieny and R. Miranda, *Phys. Rev. B: Condens. Matter*, 2009, **80**, 014415.
98 T. J. Moran, J. Nogués, D. Lederman and I. K. Schuller, *Appl. Phys. Lett.*, 1998, **72**, 617–619.
99 J. Zhu, Q. Li, J. X. Li, Z. Ding, J. H. Liang, X. Xiao, Y. M. Luo, C. Y. Hua, H. J. Lin, T. W. Pi, Z. Hu, C. Won and Y. Z. Wu, *Phys. Rev. B: Condens. Matter*, 2014, **90**, 054403.
100 G. F. Goya, T. S. Berquó, F. C. Fonseca and M. P. Morales, *J. Appl. Phys.*, 2003, **94**, 3520–3528.
101 J. Santoyo Salazar, L. Perez, O. de Abril, L. Truong Phuoc, D. Ihiawakrim, M. Vazquez, J. M. Greneche, S. Begin-Colin and G. Pourroy, *Chem. Mater.*, 2011, **23**, 1379–1386.
102 P. Dutta, S. Pal, M. S. Seehra, N. Shah and G. P. Huffman, *J. Appl. Phys.*, 2009, **105**, 07B501.
103 Ö. Özdemir, D. J. Dunlop and B. M. Moskowitz, *Geophys. Res. Lett.*, 1993, **20**, 1671–1674.
104 Y. Hwang, S. Angappane, J. Park, K. An, T. Hyeon and J. G. Park, *Curr. Appl. Phys.*, 2012, **12**, 808–811.
105 X. Zheng, C. Xu, K. Nishikubo, K. Nishiyama, W. Higemoto, W. Moon, E. Tanaka and E. Otabe, *Phys. Rev. B: Condens. Matter*, 2005, **72**, 014464.
106 S. Sako and K. Ohshima, *J. Phys. Soc. Jpn.*, 1995, **64**, 944–950.
107 S. Sako, K. Ohshima, M. Sakai and S. Bandow, *Surf. Rev. Lett.*, 1996, **03**, 109–113.
108 S. Thota, J. H. Shim and M. S. Seehra, *J. Appl. Phys.*, 2013, **114**, 214307.
109 C. R. A. Catlow and B. E. F. Fender, *J. Phys. C: Solid State Phys.*, 1975, **8**, 3267–3279.
110 M. Pasternak, R. Taylor, R. Jeanloz, X. Li, J. Nguyen and C. McCammon, *Phys. Rev. Lett.*, 1997, **79**, 5046–5049.
111 Y. Ding, J. Xu, C. T. Prewitt, R. J. Hemley, H. Mao, J. A. Cowan, J. Zhang, J. Qian, S. C. Vogel, K. Lokshin and Y. Zhao, *Appl. Phys. Lett.*, 2005, **86**, 052505.
112 A. Cabot, A. Alivisatos, V. Puntes, L. Balcells, Ò. Iglesias and A. Labarta, *Phys. Rev. B: Condens. Matter*, 2009, **79**, 094419.
113 J. Park, K. An, Y. Hwang, J. G. Park, H. J. Noh, J. Y. Kim, J. H. Park, N. M. Hwang and T. Hyeon, *Nat. Mater.*, 2004, **3**, 891–895.
114 H. K. Schmid and W. Mader, *Micron*, 2006, **37**, 426–432.
115 J. Rodríguez-Carvajal, *Physica B*, 1993, **192**, 55–69.
116 R. A. Brand, *Nucl. Instrum. Methods Phys. Res., Sect. B*, 1987, **28**, 398–416.
117 K. Binder, *Applications of Monte Carlo Methods in Statistical Physics*, Springer-Verlag, Berlin, Germany, 1984.